

RESEARCH ARTICLE

10.1029/2018JB016813

Key Points:

- Triaxial experiments on gouge-filled saw-cuts are conducted to study the role of stress field orientation on fault reactivation
- The frictional reactivation theory is experimentally validated by preexisting fault reactivation versus new shear fracture development
- Misoriented faults are weaker than theoretically predicted due to the rotation of the stress within thick fault zones

Supporting Information:

- Supporting Information S1

Correspondence to:

C. Giorgetti,
carolina.giorgetti@epfl.ch

Citation:

Giorgetti, C., Tesei, T., Scuderi, M. M., & Collettini, C. (2019). Experimental insights into fault reactivation in gouge-filled fault zones. *Journal of Geophysical Research: Solid Earth*, 124, 4189–4204. <https://doi.org/10.1029/2018JB016813>

Received 30 SEP 2018

Accepted 20 MAR 2019

Accepted article online 23 MAR 2019

Published online 18 APR 2019

Experimental Insights Into Fault Reactivation in Gouge-Filled Fault Zones

C. Giorgetti^{1,2} , T. Tesei³ , M. M. Scuderi² , and C. Collettini^{2,4} 

¹Laboratory of Experimental Rock Mechanics (LEMR), IIC-ENAC, École Polytechnique Fédérale de Lausanne, Lausanne, Switzerland, ²Dipartimento di Science della Terra, Sapienza Università di Roma, Rome, Italy, ³Rock Mechanics Laboratory, Earth Sciences Department, Durham University, Durham, UK, ⁴HP-HT Laboratory, Istituto Nazionale di Geofisica e Vulcanologia, Rome, Italy

Abstract Faults in the brittle crust constitute preexisting weakness zones that can be reactivated depending on their friction, orientation within the local stress field, and stress field magnitude. Analytical approaches to evaluate the potential for fault reactivation are generally based on the assumption that faults are ideal planes characterized by zero thickness and constant friction. However, natural faults are complex structures that typically host thick fault rocks. Here we experimentally investigate the reactivation of gouge-bearing faults and compare the resulting data with theoretical predictions based on analytical models. We simulate preexisting faults by conducting triaxial experiments on sandstone cylinders containing saw-cuts filled with a clay-rich gouge and oriented at different angles, from 30° to 80°, to the maximum principal stress. Our results show the reactivation of preexisting faults when oriented at 30°, 40°, and 50° to the maximum principal stress and the formation of a new fracture for fault orientations higher than 50°. Although these observations are consistent with the fault lock-up predicted by analytical models, the differential stress required for reactivation strongly differs from theoretical predictions. In particular, unfavorable oriented faults appear systematically weaker, especially when a thick gouge layer is present. We infer that the observed weakness relates to the rotation of the stress field within the gouge layer during the documented distributed deformation that precedes unstable fault reactivation. Thus, the assumption of zero-thickness planar fault provides only an upper bound to the stress required for reactivation of misoriented faults, which might result in misleading predictions of fault reactivation.

1. Introduction

Reactivation of preexisting faults in the brittle crust occurs when the shear stress acting on a fault overcomes its strength (e.g., Copley, 2017; Sibson, 1985). A reliable estimate of fault strength and potential for reactivation are crucial in the assessment of seismic hazard (e.g., Harris & Simpson, 1992; Sumy et al., 2014). In the last decade, increasing attention has focused on the reactivation of preexisting faults due to stress field perturbation during fluid injection (e.g., Gan & Elsworth, 2014; Moeck et al., 2009; Rutqvist et al., 2007; Streit & Hills, 2004). This is because this procedure possibly causes induced seismicity (e.g., Ellsworth, 2013; Schoenball et al., 2018; Walsh & Zoback, 2016) and hydrocarbon leaks from traps (e.g., Wiprut & Zoback, 2002). Analytical approaches are often used to evaluate the potential for reactivation in both natural (e.g., Bolognesi & Bistacchi, 2016; Collettini & Trippetta, 2007; Leclère & Fabbri, 2013; Lisle & Srivastava, 2004; Sibson, 1985) and induced stress field perturbations (e.g., Gan & Elsworth, 2014; Moeck et al., 2009). These approaches consider faults as zero-thickness planes embedded in a homogenous and elastic medium. Consequently, the differential stress required for reactivation depends on fault friction, maximum principal stress orientation, and minimum effective principal stress magnitude (e.g., Jaeger, 1960; Morris et al., 1996; Sibson, 1985). Furthermore, the strength of the surrounding rocks poses an additional limitation to the maximum differential stress required for reactivation at a given minimum principal stress (e.g., Jaeger, 1960). The predictions resulting from these analytical models have been successfully validated by triaxial experiments on foliated anisotropic rocks (i.e., gneiss, schist, slate, and shale; e.g., Donath, 1961; Hoek, 1964; Jackson & Dunn, 1974; Jaeger, 1960; McLamore & Gray, 1967; McCabe & Koerner, 1975; Shea & Kronenberg, 1993) and triaxial saw-cut experiments on bare surfaces (e.g., Hayward & Cox, 2017; Jackson & Dunn, 1974), where foliation and bare surfaces can be confidently considered as zero-thickness planes.

Although considered planes at the crustal scale, mature faults are complex structures hosting fault cores up to several hundred meters thick (e.g., Ben-Zion & Sammis, 2003; Caine et al., 1996; Faulkner et al., 2011; Shipton et al., 2006), which can be significantly weaker than the surrounding rocks (e.g., Collettini et al., 2009; Lacroix et al., 2015). Theoretical and experimental observations suggest that the presence of a weak gouge layer along a fault results in the rotation of the stress field in proximity to the fault (e.g., Byerlee & Savage, 1992; Gu & Wong, 1994; Lecomte et al., 2011; Lockner & Byerlee, 1993; Mandl et al., 1977; Rice, 1992), influencing fault reactivation and possibly enhancing slip on unfavorably oriented faults (Lecomte et al., 2012). Notably, a fault gouge experiencing distributed deformation behaves as a Coulomb material, within which the maximum principal stress rotates to an angle of 45° to the fault boundaries (e.g., Byerlee & Savage, 1992; Lockner & Byerlee, 1993; Mandl et al., 1977). Thus, the remaining key questions are as follows: how does the rotation of the far-field stress influence fault reactivation and are the analytical models applicable to thick, gouge-bearing fault zones? Here we aim at addressing these questions by conducting triaxial experiments with gouge-filled saw-cuts oriented at different angles to the maximum principal stress.

1.1. Theoretical Background: The Single Plane of Weakness Theory

The simplest theory used to predict frictional fault reactivation is the single plane of weakness theory (e.g., Jaeger, 1960), which is a generalization of the Coulomb-Mohr failure criterion. In this theoretical framework, the minimum differential stress, $\sigma_d = \sigma_1 - \sigma_3$, required for frictional reactivation of a preexisting cohesionless fault is defined as follows (e.g., Sibson, 1985):

$$\sigma_d = \frac{1 + \mu_s \cot \theta}{1 - \mu_s \tan \theta} \sigma_3 - \sigma_3 \quad (1)$$

where σ_3 is the minimum principal stress, μ_s is the sliding friction of the preexisting fault, and θ is the frictional reactivation angle, which is the angle between the fault and the maximum principal stress σ_1 . The frictional lock-up occurs when the σ_d approaches infinity, that is when $\theta = \tan^{-1}(\mu^{-1})$. Moreover, frictional reactivation occurs when the differential stress required for fault reactivation (equation (1)) is lower than the differential stress required for the failure of the surrounding rock. The differential stress required for failure, and thus the upper bound of the differential stress for reactivation, depends on the rock strength, which consists of the angle of internal friction, φ_i , and the cohesion, c , and on the minimum principal stress, σ_3 , as follows:

$$\sigma_d = \frac{2c \cos \varphi_i + 2\sigma_3 \sin \varphi_i}{1 - \sin \varphi_i} \quad (2)$$

2. Methods

We studied the reactivation of gouge-bearing faults that are experimentally simulated by a layer of gouge sandwiched between intact rock blocks and placed at different angles θ to the maximum principal stress. The experiments were designed to investigate the reactivation of preexisting faults that are weaker relative to the host rock. To ensure this, we used a clay-rich gouge derived from the Marne a Fucoidi formation outcropping in the northeastern limb of the Monte Montiego anticline in the Northern Apennines of Italy (Giorgetti et al., 2016), where this formation constitutes an important décollement level (e.g., Barchi et al., 2001). The gouge is composed of 59 wt % of CaCO_3 constrained by calcimetry (Giorgetti et al., 2016), and the remaining percentage consists of a clay mineral assemblage of smectite, illite, and mixed layer illite-smectite (~50% smectite, ~30% illite, and ~20% mixed layer illite-smectite; Coccioni et al., 1989). The experimental fault is embedded within a lithic arkose sandstone (*Pietraserena* sandstone, e.g., Fratini et al., 2014).

To investigate how the presence of gouge affects fault reactivation and to fully constrain the mechanical properties of the involved lithologies, triaxial saw-cut experiments have been complemented by two sets of experiments with the following configurations (Table 1): (1) uniaxial and triaxial experiments conducted on intact cylindrical samples of *Pietraserena* sandstone to characterize the strength of the rock surrounding

Table 1
List and Details of the Experiments

Experiment number	Configuration	Saw-cut angle to sample axis ^a	Layer thickness h^b (mm)	Material	Confining pressure/normal stress (MPa)	Displacement rate ^c ($\mu\text{m/s}$)
b654	uniaxial	-	-	Pietraserena sandstone	$P_c = 0$	$v_a = 0.1$
b655	uniaxial	-	-	Pietraserena sandstone	$P_c = 0$	$v_a = 0.1$
b565	triaxial	-	-	Pietraserena sandstone	$P_c = 10$	$v_a = 0.1$
b584	triaxial	-	-	Pietraserena sandstone	$P_c = 20$	$v_a = 0.1$
b585	triaxial	-	-	Pietraserena sandstone	$P_c = 30$	$v_a = 0.1$
b652	triaxial	-	-	Pietraserena sandstone	$P_c = 15$	$v_a = 0.1$
b653	triaxial	-	-	Pietraserena sandstone	$P_c = 25$	$v_a = 0.1$
b599	double-direct shear	-	3	clay-rich marl	$\sigma_n = 10 - 20 - 30^d$	$v_s = 0.5$
b662	double-direct shear	-	3	clay-rich marl	$\sigma_n = 30$	$v_s = 0.4$
b663	double-direct shear	-	3	clay-rich marl	$\sigma_n = 30$	$v_s = 0.4$
b670	double-direct shear	-	3	clay-rich marl	$\sigma_n = 50$	$v_s = 0.4$
b586	triaxial saw-cut	30°	3	Pietraserena sandstone + clay-rich marl	$P_c = 10$	$v_a = 0.3$
b588	triaxial saw-cut	60°	3	Pietraserena sandstone + clay-rich marl	$P_c = 10$	$v_a = 0.3$
b596	triaxial saw-cut	50°	3	Pietraserena sandstone + clay-rich marl	$P_c = 10$	$v_a = 0.3$
b597	triaxial saw-cut	40°	3	Pietraserena sandstone + clay-rich marl	$P_c = 10$	$v_a = 0.3$
b598	triaxial saw-cut	70°	3	Pietraserena sandstone + clay-rich marl	$P_c = 10$	$v_a = 0.3$
b610	triaxial saw-cut	40°	3	Pietraserena sandstone + clay-rich marl	$P_c = 10$	$v_a = 0.3$
b611	triaxial saw-cut	50°	3	Pietraserena sandstone + clay-rich marl	$P_c = 10$	$v_a = 0.3$
b617 ^e	triaxial saw-cut	50°	3	Pietraserena sandstone + clay-rich marl	$P_c = 10$	$v_a = 0.3$
b619 ^f	triaxial saw-cut	50°	3	Pietraserena sandstone + clay-rich marl	$P_c = 10$	$v_a = 0.3$
b628	triaxial saw-cut	50°	1	Pietraserena sandstone + clay-rich marl	$P_c = 10$	$v_a = 0.3$
b629	triaxial saw-cut	50°	5	Pietraserena sandstone + clay-rich marl	$P_c = 10$	$v_a = 0.3$
b646	triaxial saw-cut	80°	3	Pietraserena sandstone + clay-rich marl	$P_c = 10$	$v_a = 0.3$
b648	triaxial saw-cut	70°	3	Pietraserena sandstone + clay-rich marl	$P_c = 10$	$v_a = 0.3$

^aApplicable only to triaxial saw-cut configuration. ^bApplicable only to double-direct-shear and triaxial saw-cut configuration. ^cAxial velocity (v_a) in triaxial and triaxial saw-cut experiments and sliding velocity (v_s) in double-direct-shear experiments. ^dThe experiment consists in three shearing phases (shear loading-unloading) conducted at progressively higher normal stress values. ^e2.75-mm total displacement along the saw-cut to collect microstructures. ^f1.50-mm total displacement along the saw-cut to collect microstructures.

the fault; (2) biaxial friction experiments on the clay-rich marly gouge to characterize the frictional strength of the fault.

Experiments were conducted using a servo-controlled biaxial apparatus (BRAVA, Brittle Rock deformation Versatile Apparatus) equipped with a pressure vessel (Collettini et al., 2014, for further details; Figure 1a). The vertical and horizontal pistons were used to apply forces, which are measured using strain-gauged load cells located within the vessel with ± 0.03 -kN accuracy. Vertical and horizontal load point displacements are measured using linear variable differential transformer (LVDT) sensors with ± 0.1 - μm accuracy. The servo-hydraulic system can be controlled in either pressure feedback, to maintain a constant force, or displacement feedback, to advance the piston at a constant displacement rate. The pressure intensifier, connected to the pressure vessel, applies the confining pressure via paraffinic oil. The pressure vessel is equipped with two doors sealed with O-rings to prevent confining oil leakage. The confining pressure is measured through pressure transducers with ± 7 -kPa accuracy and controlled via a pressure-feedback control mode.

2.1. Double-Direct-Shear Experiments

Friction experiments were performed in double-direct-shear configuration, in which two layers of clay-rich gouge were placed between three grooved forcing blocks (Figure 1b). The gouge was prepared from outcropping clay-rich marls (Giorgetti et al., 2016), which were crushed and sieved to < 125 - μm grain size. The two gouge layers, each with an initial ~ 3 -mm uniform thickness, were constructed to have a $5 \text{ cm} \times 5 \text{ cm}$ area, which is maintained constant throughout the experiment. Experiments were performed at room temperature and under dry (i.e., room humidity) conditions.

To evaluate the reactivation criterion, we conducted experiments at different normal stress σ_n ranging between 10 and 50 MPa (Figure 1b). The normal stress was first applied and maintained constant

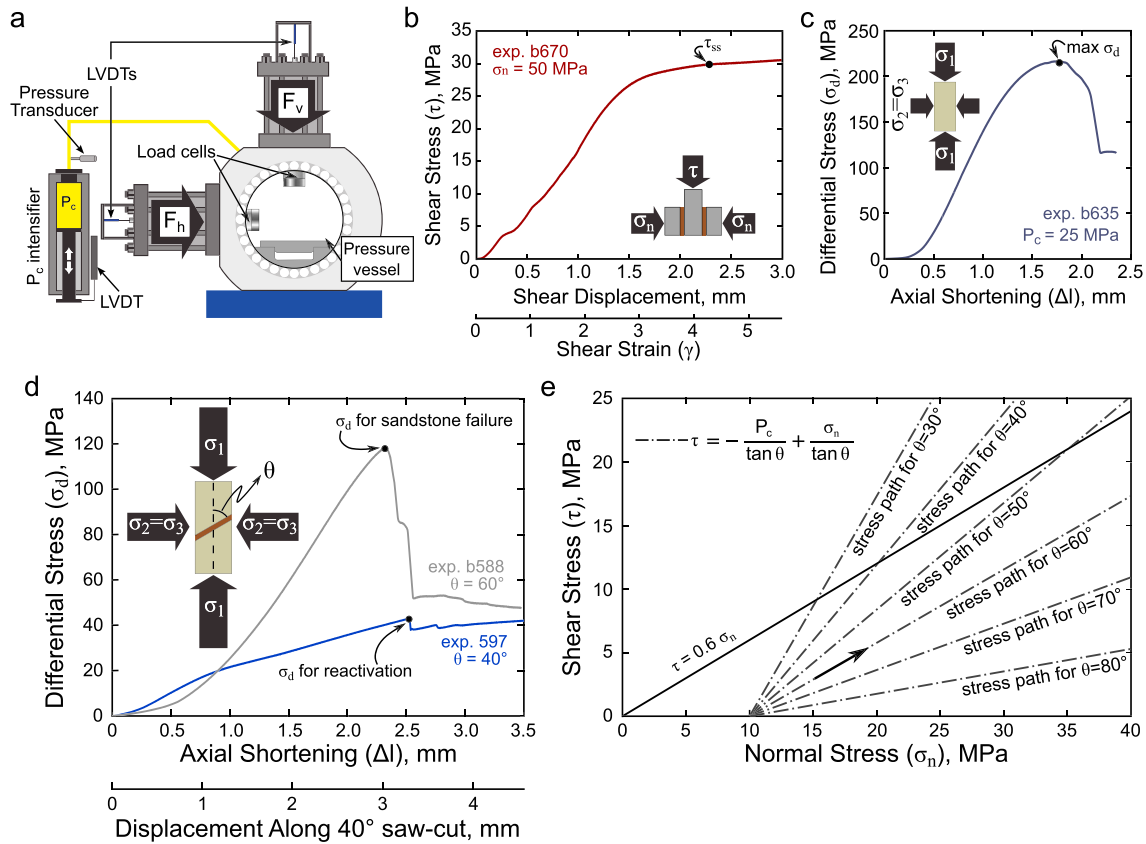


Figure 1. The BRAVA (Brittle Rock deformation Versatile Apparatus) rock deformation apparatus (after Scuderi & Colletini, 2016). (a) Experimental apparatus (see text for details). (b) Evolution of shear stress plotted versus shear displacement and strain during a friction experiment. τ_{ss} indicates the point at which the shear stress value to estimate the sliding friction is picked. The inset shows the double-direct-shear configuration. (c) Evolution of differential stress plotted versus axial displacement for a triaxial experiment. The black dot shows where the differential stress value to estimate failure strength is picked. The inset shows the triaxial configuration. (d) Evolution of differential stress plotted versus axial displacement during triaxial saw-cut experiments. The uppermost curve shows the evolution of differential stress during an experiment in which the sample deformed through the development of a new fracture, whereas the lowermost curve shows the evolution of differential stress during an experiment in which the sample deformed through the reactivation of the saw-cut. The black dots show how σ_d for data discussion is picked. The inset shows the triaxial saw-cut configuration. (e) Predicted stress paths experienced by saw-cuts oriented at different angles to the maximum principal stress, assuming a constant confining pressure of 10 MPa.

throughout the experiment. Then, the shear stress was applied by advancing the vertical piston at a constant velocity of 0.4 or 0.5 $\mu\text{m/s}$. The values of shearing velocity were chosen to be comparable with the along saw-cut shearing velocities for reactivated orientations. The displacement values of the vertical and horizontal load points were corrected for the elastic stretch of each load frame, taking into account that the machine stiffness is 1,283 kN/mm on the horizontal axis and 928.5 kN/mm on the vertical axis.

In brittle fault reactivation, according to the Amontons-Coulomb friction law, the shear stress τ linearly depends on the applied normal stress σ_n (e.g., Bowden & Tabor, 1950; Jaeger & Cook, 1979) as follows:

$$\tau = \mu_s \sigma_n \quad (3)$$

where the sliding friction is a function of the angle of sliding friction φ_s , that is, $\mu_s = \tan(\varphi_s)$. We measured the shear stress at the onset of steady state sliding (τ_{ss} in Figure 1b) to estimate the sliding friction of the marly gouge at low strain conditions.

2.2. Uniaxial and Triaxial Experiments

In the following, we describe uniaxial experiments as a particular case of triaxial experiments in which confining pressure is $P_c = 0$ MPa. Triaxial experiments were conducted on cylindrical samples 37–38 mm in diameter and 80–88 mm in height (i.e., 2:1 minimum aspect ratio, Paterson & Wong, 2005). Intact samples for

standard uniaxial and triaxial tests were 80 to 83-mm height, whereas gouge-bearing saw-cut samples were 83 to 88-mm height. Triaxial saw-cut experiments were conducted systematically changing the orientation of the saw-cut, that is, the angle θ between the experimental fault and the maximum principal stress, in the range $\theta = 30\text{--}80^\circ$. The samples were prepared by cutting Pietrasarena sandstone cylinders into two pieces at given θ angles. The saw-cut surfaces were roughened with #60 grit SiC abrasive paper (265- μm average abrasive grain size) to ensure frictional sliding to occur within the gouge layer (for further details on roughness characterization see Table S1 and Figure S1 in the supporting information). For all the tested orientations (Table 1), an initial $\sim 3\text{-mm}$ thick layer of marly gouge was placed within the saw-cut surface. To test the effect of layer thickness on the mechanics of reactivation, we performed further experiments at $\theta = 50^\circ$ with an initial layer thickness of ~ 1 and ~ 5 mm, respectively. The marly gouge is the same gouge that was sheared in friction experiments (see section 2.1). The samples (intact rock or intact rock + gouge layer) were placed between two stainless steel end platens, eventually jacketed with one (standard triaxial experiment) or two (triaxial saw-cut experiment) layers of polyolefin heat-shrink tube, and sealed with steel wires at the extremities to avoid confining oil leakage. Experiments were performed at room temperature and under dry (i.e., room humidity) conditions.

To evaluate the failure envelope, we performed experiments on intact samples at different values of confining pressure P_c , in the range $P_c = 0\text{--}30$ MPa (e.g., Figure 1c). Saw-cut experiments were conducted at $P_c = 10$ MPa (Figure 1d) (Table 1). The following loading procedure was performed during the experiments. Confining pressure was first applied and maintained constant throughout the experiment. The differential stress was then applied by advancing the vertical piston at a constant velocity of $0.1 \mu\text{m/s}$, corresponding to axial strain rates of $1.2 \times 10^{-6} \text{ s}^{-1}$, and $0.3 \mu\text{m/s}$, respectively, for standard triaxial and triaxial saw-cut experiments. Thus, the stress field acting on the sample is $\sigma_2 = \sigma_3 = P_c$, where σ_3 and σ_2 are the minimum and intermediate principal stresses, respectively, and the maximum principal stress $\sigma_1 = P_c + \sigma_d$, where σ_d is the differential stress measured by the load cell located inside the pressure vessel. The values of the vertical load point displacement were corrected for the machine stiffness on the vertical axis which, depending on the confining pressure, ranges between 757.7 and 771.2 kN/mm.

In standard triaxial experiments, the maximum differential stress preceding a brittle shear failure linearly depends on the confining pressure (e.g., Paterson & Wong, 2005) and the linear correlation coefficients between σ_d and P_c define the angle of internal friction φ_i and the cohesive strength c (e.g., Wood, 1990) as follows (for equation derivation see Text S1 in the supporting information):

$$\sigma_d = \frac{6 \sin \varphi_i}{3 - 3 \sin \varphi_i} P_c + \frac{6 \cos \varphi_i}{3 - 3 \sin \varphi_i} c \quad (4)$$

From equation (4), we evaluated the failure strength through the Coulomb failure criterion (Coulomb, 1776):

$$\tau = \mu_i \sigma_n + c \quad (5)$$

where τ is the shear stress, σ_n is the normal stress on the failure plane, and $\mu_i = \tan(\varphi_i)$ is the internal friction of the intact rock.

In triaxial saw-cut experiments (Figure 1d), differential stress was corrected for jacket strength (i.e., 0.56 MPa/mm) and for the reduction in contact area during saw-cut reactivation. When shear occurs within the saw-cut, the contact area continuously changes (e.g., Scott, Lockner, et al., 1994), as follows:

$$A = r^2(\Theta - \sin \Theta), \quad \Theta = \pi - 2 \sin^{-1} \left(\frac{\Delta l}{2r} \tan \theta \right) \quad (6)$$

where Δl is the axial displacement and r is the radius of the cylindrical sample. Θ is the angle subtended by the points of intersection of two overlapping circles of radius r and whose centers distance is $\Delta l \tan \theta$, at the center of the circles. The normal stress acting on the gouge layer is a function of the differential stress σ_d , the angle θ , and the confining pressure P_c . The shear stress acting on the gouge layer is a function of the differential stress σ_d and the angle θ . At constant P_c and θ , the stresses resolved on a saw-cut evolve depending on the differential stress as follows:

$$\sigma_n = \frac{\sigma_d(1 - \cos 2\theta) + 2P_c}{2} \quad (7)$$

$$\tau = \frac{\sigma_d \sin 2\theta}{2} \quad (8)$$

Consequently, under the constant confining pressure of 10 MPa, saw-cuts oriented at different θ angles undergo different stress paths in a $\tau - \sigma_n$ plane (Figure 1e).

Additional experiments with different total amounts of displacement along a saw-cut oriented at $\theta = 50^\circ$ (i.e., 1.5, 2.75, and 6 mm) were performed to investigate the evolution of shear localization during fault reactivation.

Thin sections parallel to the sense of shear were realized by collecting and embedding in epoxy resin the gouge layer at the end of triaxial saw-cut experiments. Microstructural observations were performed with a scanning electron microscope FEI Quanta 400 installed at the Scanning Electron Microscope Laboratory of the Earth Sciences Department at Sapienza University of Rome (Italy) and a JEOL JSM-6500F thermal field emission scanning electron microscope installed at the Electron Microscopy Laboratory at the INGV in Rome (Italy). All the microphotographs presented are backscattered electron images. The analyses were performed using an acceleration voltage of 15 or 30 kV, a working distance of 10 or 11 mm, and carbon or gold coating.

3. Results

3.1. Marl Friction and Sandstone Strength

Figure 2a summarizes the results for friction experiments on the clay-rich marly gouge. The shear stress, picked at the onset of the steady state sliding (Figure 1b), is linearly dependent on normal stress (Figure 2a), consistent with the Amontons-Coulomb friction law (equation (3)). The apparent friction, calculated as the slope of the best fit line in shear stress versus normal stress plot, is $\mu_s = 0.59$. Sliding friction of gouges is commonly evaluated via the Coulomb-Mohr criterion (Figure 2a; equation (3)), based on the assumption that the deformation is localized along a thin through-going shear zone that is active during steady state frictional sliding in direct-shear experiments (e.g., Logan et al., 1992; Marone et al., 1992; Tchalenko, 1970). However, in the case of distributed deformation the maximum principal stress rotates at 45° to the gouge boundaries (e.g., Mandl et al., 1977; Marone et al., 1992) and thus, the best fit line on shear stress versus normal stress plot has a slope equal to $\tan^{-1}[\sin(\varphi_s)]$ (Figures 2a and 2b, e.g., Marone et al., 1992; Scott, Marone, et al., 1994). The two friction values, estimated as $\tan^{-1}(\varphi_s)$ and $\tan^{-1}(\sin[\varphi_s])$, represent the two end-members for purely localized and purely distributed deformation, respectively, and mixed-mode deformation could result in intermediate friction values. During our double-direct-shear gouge experiments microstructural observations show that the deformation is still highly distributed (Figure S2 in supporting information), as also supported by the slight strain hardening trend characterizing the steady state (Figures 1b S2 in the supporting information). Therefore, we suggest that the assumption of distributed deformation is most appropriate, especially at the onset of the steady state sliding where the shear stress was picked, and the friction coefficient of the gouge is $\mu_r = \sin(\varphi_s) = 0.73$.

Figure 2c summarizes the results for triaxial experiments on intact Pietraserena sandstone. The evolution of differential stress σ_d with progressive axial shortening (Δl) exhibits brittle behavior (Figure 1c, e.g., Paterson & Wong, 2005; Wong et al., 1997), as shown by stress drop and localized shear fractures in failed samples. The peak differential stress shows a linear increase with confining pressure (Figure 2c), further indicating pressure-sensitive brittle behavior (e.g., Paterson & Wong, 2005). The coefficients of internal friction and the cohesion, estimated via the best fit line of peak σ_d versus P_c (equation (4)), are $\mu_i = 0.60$ and $c = 45.19$ MPa, respectively.

Thus, analytical predictions for fault reactivation versus new fault development (Figure 2d, equations (1) and (2); Jaeger, 1960) are built on the grounds of (1) the friction coefficient of the clay-rich gouge filling the saw-cut, that is, the fault rock (Figures 2a and 2b); and (2) the failure strength of Pietraserena sandstone, that is, the fault wall rock (Figure 2c).

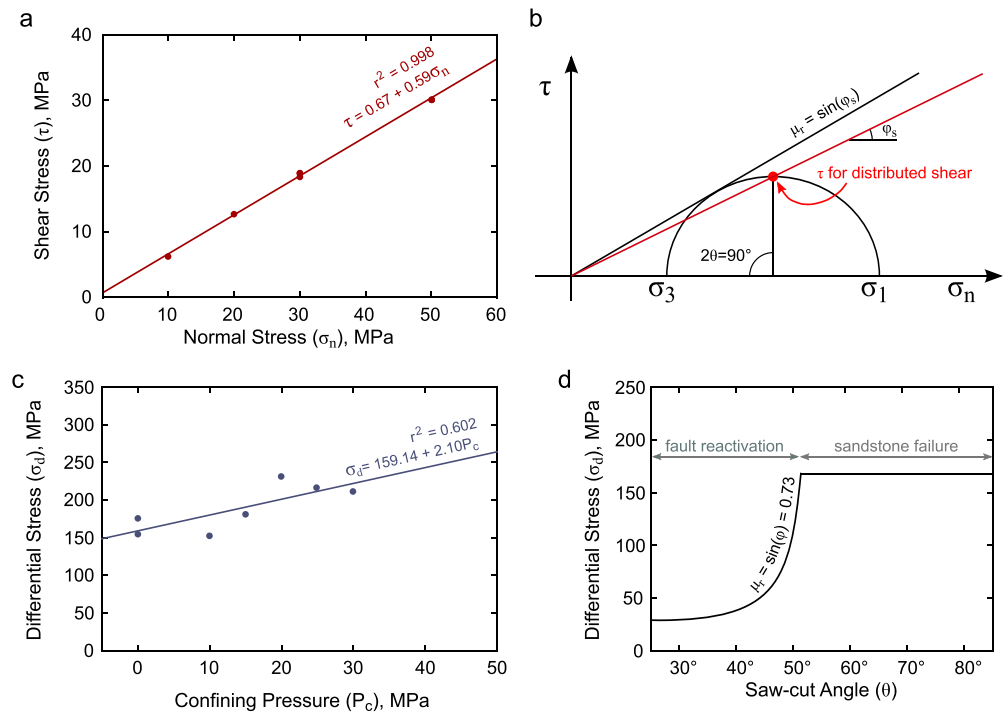


Figure 2. (a) Results from double-direct-shear friction experiments on clay-rich marly gouges. The shear stress at the onset of steady state sliding (Figure 1b) is plotted against normal stress. Linear regression results in sliding friction $\mu_s = 0.59$ and almost zero cohesion. (b) Stress state in the gouge layer in the case of distributed (red line) versus localized (black line) deformation. At the low strains of our experiments, the gouge deforms via distributed shear (Figure S2 in supporting information) and this results in the rotation of the maximum principal stress at 45° to the gouge boundaries and $\mu_r = \sin(\varphi_s) = 0.73$. (c) Results from uniaxial and triaxial experiments on Pietraserena sandstone. Peak differential stress is plotted against confining pressure. Linear regression results in an angular coefficient of 2.10 and an intercept of 159.14 MPa (equation (4)). The $r^2 = 0.602$ is likely due to heterogeneities in the sandstone strength. (d) Analytical model (equations (1) and (2)) based on the Pietraserena sandstone strength ($\mu_i = 0.60$ and $c = 45.19$ MPa, equation (4); Figure 2c) and the clay-rich marl friction based on the assumption of distributed deformation during double-direct-shear experiments ($\mu_r = 0.73$, Figures 2a and 2b).

3.2. Fault Reactivation Versus New Fracture Development in Triaxial Saw-Cut Experiments

Results from triaxial saw-cut experiments exhibit two different deformation mechanisms depending on the saw-cut angle. Samples with saw-cuts at $\theta = 60^\circ$ – 70° – 80° deformed through the development of new fractures (Figure 3), whereas reactivation occurs during the deformation of samples containing saw-cuts at $\theta = 30^\circ$ – 40° – 50° (Figure 4).

3.2.1. New Fracture Development: Mechanical Data

Figure 3 summarizes the mechanical data from saw-cut samples with a 3-mm-thick layer at $\theta = 60^\circ$ – 70° – 80° and $P_c = 10$ MPa. The σ_d versus Δl curves show an evolution that is typical of brittle deformation (Figure 3a, e.g., Paterson & Wong, 2005; Wong et al., 1997), as further suggested by the development of localized fractures (Figure 3b). The quasi-linear elastic phase of loading is characterized by a modulus that tends to increase with increasing θ angle. During the failure, we observe two or more stress drops separated by short strain-weakening stages. At the end of the experiment, visual inspection of the resulting samples shows a through-going fault in association with conjugate fractures that end at the boundary of the weak layer (Figure 3b).

The peak differential stress before failure ranges between 118 and 176 MPa, without showing any systematic variation with the angle θ . The sample containing the 60° saw-cut failed at the lowest observed σ_d value, and the two samples containing the 70° saw-cut show a difference of 41 MPa in peak σ_d . This variability could be ascribed to the strength heterogeneity characterizing the lithic arkose sandstone (Figure 2c).

3.2.2. Fault Reactivation: Mechanical Data

When preexisting faults reactivate (Figure 4a), the evolution of differential stress with increasing displacement shows three main stages for the ~3-mm-thick gouge layers (Figures 4b and 4c): (1) an initial stress

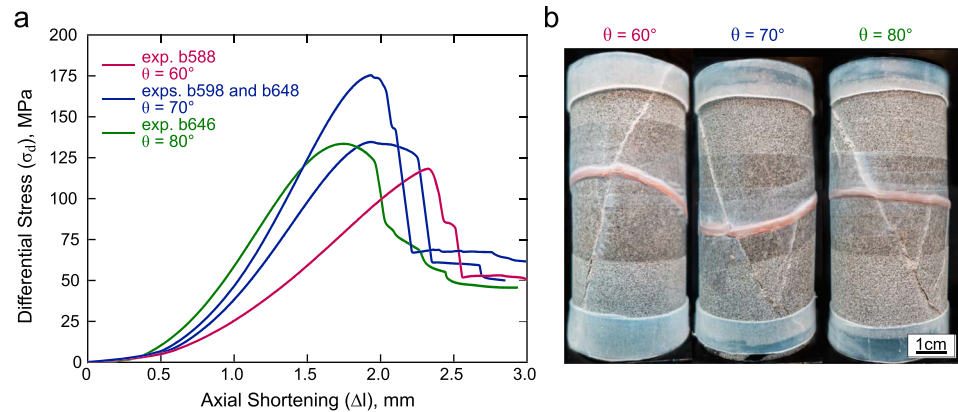


Figure 3. (a) Evolution of differential stress plotted versus axial shortening during triaxial saw-cut experiments with 3-mm-thick gouge layers at $\theta = 60^\circ$, $\theta = 70^\circ$, and $\theta = 80^\circ$. With increasing displacement, the differential stress is characterized by an initial increase until the achievement of a peak stress value followed by two or more stress drops separated by short strain-weakening stages. Peak differential stress does not systematically depend on θ angle. The slope of the linear elastic loading portion of the curve increases with increasing θ , suggesting that saw-cut orientation influences the sample bulk elasticity. (b) Through-going faults develop during triaxial saw-cut experiments at $\theta = 60^\circ$ – 70° – 80° . These major structures are associated with minor conjugate fractures, which end at the boundary of the weak layer.

versus displacement evolution that is typical of rocks failing in compression, that is, comprising initial porosity closure, elastic loading, and yielding (e.g., Brace et al., 1966; Jaeger & Cook, 1979) (stage I); (2) an almost linear strain hardening (stage II); and (3) one or more stress drops progressively dampened until stable sliding is achieved (stage III). With increasing θ from 30° to 50° , the strain hardening (stage II) is progressively larger, resulting in an overall higher σ_d required to promote the first stress drop (Figure 4c). At $\theta = 30^\circ$, the first stress drop is small ($\Delta\sigma_d \approx 1.5$ MPa), whereas at $\theta = 40^\circ$ – 50° the stress drop is significantly larger ($\Delta\sigma_d \approx 4.5$ – 6.8 MPa, Figure 4c). During stage III, after the initial stress drops the differential stress required for stable sliding increases with progressive displacement depending on the θ , from a subtle trend at 30° to an evident trend at 50° .

Figure 4d shows the effect of gouge layer thickness on saw-cut reactivation at $\theta = 50^\circ$. The differential stress supported by the sample systematically decreases with increasing thickness of the gouge layer. The deformation of the 1-mm-thick layer occurs at differential stress values that are almost twice the values required for the reactivation of the 5-mm-thick layer (Figure 4d). Additionally, the experiment with the 5-mm-thick layer does not show a clear distinction between stages I and II (Figure 4d).

3.2.3. Fault Reactivation: Microstructures

Microstructural investigations, conducted on sheared 3-mm-thick layers at $\theta = 50^\circ$ and $P_c = 10$ MPa, give insights into the micromechanical processes occurring during fault gouge reactivation (Figure 5a). After 1.5 mm of displacement along the saw-cut (i.e., during stage I), the microstructure is characterized by clasts of marl homogeneously distributed in a fine and porous matrix composed of clay flakes and calcite grains (Figures 5b and 5c). The clasts have heterogeneous grain size, typically between 20 and 100 μm , and are constituted by rounded calcareous microfossils and by clasts with an irregular boundary that consist of aggregates composed of calcareous nanofossils and clay flakes (i.e., marly clasts, Figure 5c).

With increasing shear displacement, up to 2.75 mm (i.e., during stage II), the experimental fault gouge becomes increasingly denser and homogeneous. Although the deformation is still distributed, we observe few decompression cracks oriented parallel and at low angles to the boundary, possibly developed during sample unloading and recovery. These cracks suggest the incipient development of boundary and synthetic Riedel shear bands (Figure 5d). The boundaries of the marly clasts are smoother than in stage I. Elongated clasts, both calcareous microfossils, and marly aggregates are often observed imbricated parallel to the incipient Riedels, according to the shear direction (Figures 5d–5e).

At the end of stage III, after a shear displacement of ~ 6 mm, the deformation is localized along shear bands parallel and at a low angle to the saw-cut, that is, boundary and Riedel shears, respectively (Figures 5f–5g; Logan et al., 1992). These shear bands are characterized by the absence of marly aggregates, which are

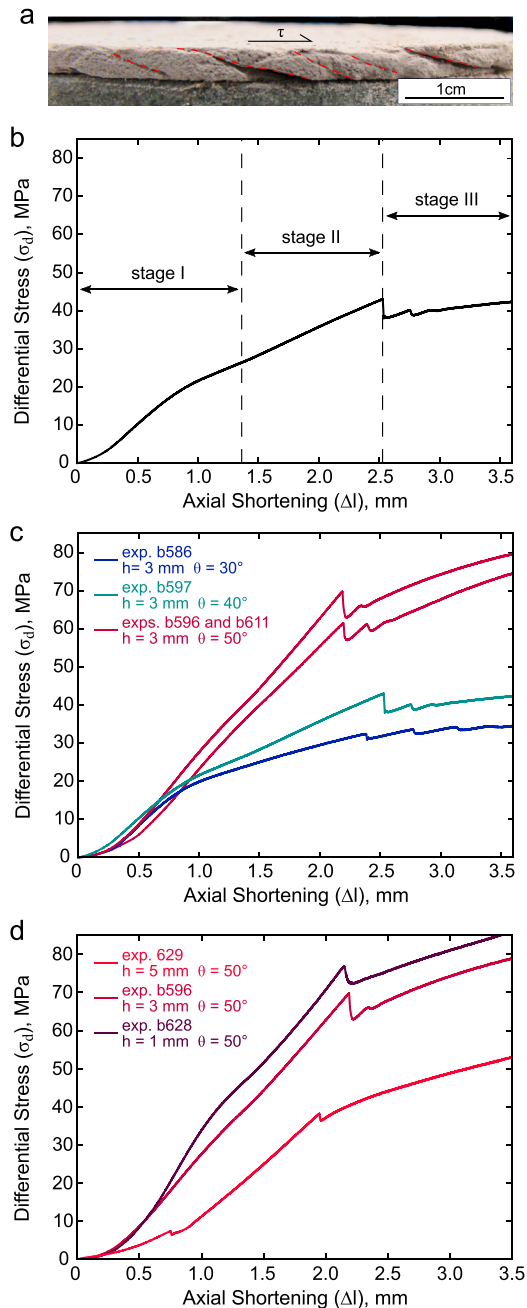


Figure 4. Results from triaxial saw-cut experiments in which deformation occurs via saw-cut reactivation. (a) Sheared gouge at the end of a triaxial saw-cut experiment showing Riedel shear bands (red dashed lines). (b) Characteristic evolution curve of differential stress versus axial displacement during the reactivation of saw-cuts with 3-mm-thick gouge layers (exp. b597). During stage I the stress versus displacement evolution suggests initial porosity closure, elastic loading, and yielding. During stage II the stress increases linearly. During stage III the stress evolves through progressively dampened stress drops to stable sliding. (c) Differential stress plotted versus axial displacement for 3-mm-thick saw-cuts at different orientations to the maximum principal stress. The slope of stage II increases with increasing saw-cut angle. (d) Differential stress plotted versus axial displacement for saw-cut samples characterized by different layer thickness at $\theta = 50^\circ$. The differential stress supported by the sample strongly decreases with increasing layer thickness.

instead present in the surrounding gouge (Figure 5f). The fine-grained gouge along boundary and Riedel shear bands derives from the disaggregation of marly clasts and comminution of calcite grains.

4. Discussion

4.1. Integration of Mechanical Data and Microstructures During Saw-Cut Reactivation

Saw-cut experiments with $\theta = 30^\circ$ – 40° – 50° show that the reactivation occurs with peculiar stress versus displacement evolution. By integrating mechanical data and microstructures, we propose the following micromechanical evolution of the fault during reactivation. Following sample yielding occurring within stage I and during the strain hardening in stage II, the fault gouge evolves from a loosely packed and randomly oriented fabric to a densely packed state with incipient localization bands, as documented by the difference between microstructures after 1.5 (stage I) and 2.75 mm of displacement (stage II, Figures 5b and 5c versus Figures 5d and 5e; e.g., Logan et al., 1992). This evidence suggests that irreversible gouge deformation commences via shear-enhanced compaction and porosity reduction occurring via distributed granular and potentially cataclastic flows, characterized by the partial comminution of calcareous microfossils and the disaggregation of marly clasts. This shear-enhanced compaction is more efficient within misoriented faults resulting in steeper strain hardening. Specifically, while loading via increasing σ_1 , the misoriented fault at 50° is subject to normal stress increments that are higher relative to the corresponding shear stress increments (Figure 1e). Thus, the progressive mean stress increase is more pronounced in faults lying at high angles to σ_1 , resulting in higher compaction. Once the gouge is effectively compacted elastic energy can be stored and then released during the stress drop at the end of stage II. We interpret the sudden unstable slip associated with the first stress drop as the full reactivation of the fault and the differential stress right before the stress drop as the maximum stress supported by the fault before reactivation. During stage II, the retrieved microstructures are characterized by Riedel- and boundary-oriented stress relaxation fractures (Figures 5d and 5e), suggesting that the localization of stress and the establishment of granular force chains occur before the stress drop (e.g., Benson et al., 2007; Lockner et al., 1992; Thompson et al., 2006). This inhomogeneous stress distribution occurs in the absence of localized grain size reduction and thus potentially favors granular dilatancy followed by stress release and sudden unstable fault slip (e.g., Biegel et al., 1989; Thompson & Grest, 1991).

After the initial stress drops, fault slip proceeds via stable sliding within increasingly localized shear bands undergoing cataclastic and granular flow, as demonstrated by the occurrence of thin Riedel and boundary shears (Figures 5f and 5g). The strong differential stress increase with increasing displacement occurring during stage III in misoriented faults at high angles to σ_1 (Figures 4c and 4d), which is absent in well-oriented faults, possibly results from the different stress paths, and thus mean stress increments, experienced by the faults (Figure 1e).

4.2. Fault Reactivation: Theory Versus Experimental Data

Figure 6 compares the analytically predicted (Figure 2d) and the experimentally derived values of differential stress for both fault reactivation and new failure development as a function of the θ angle. The

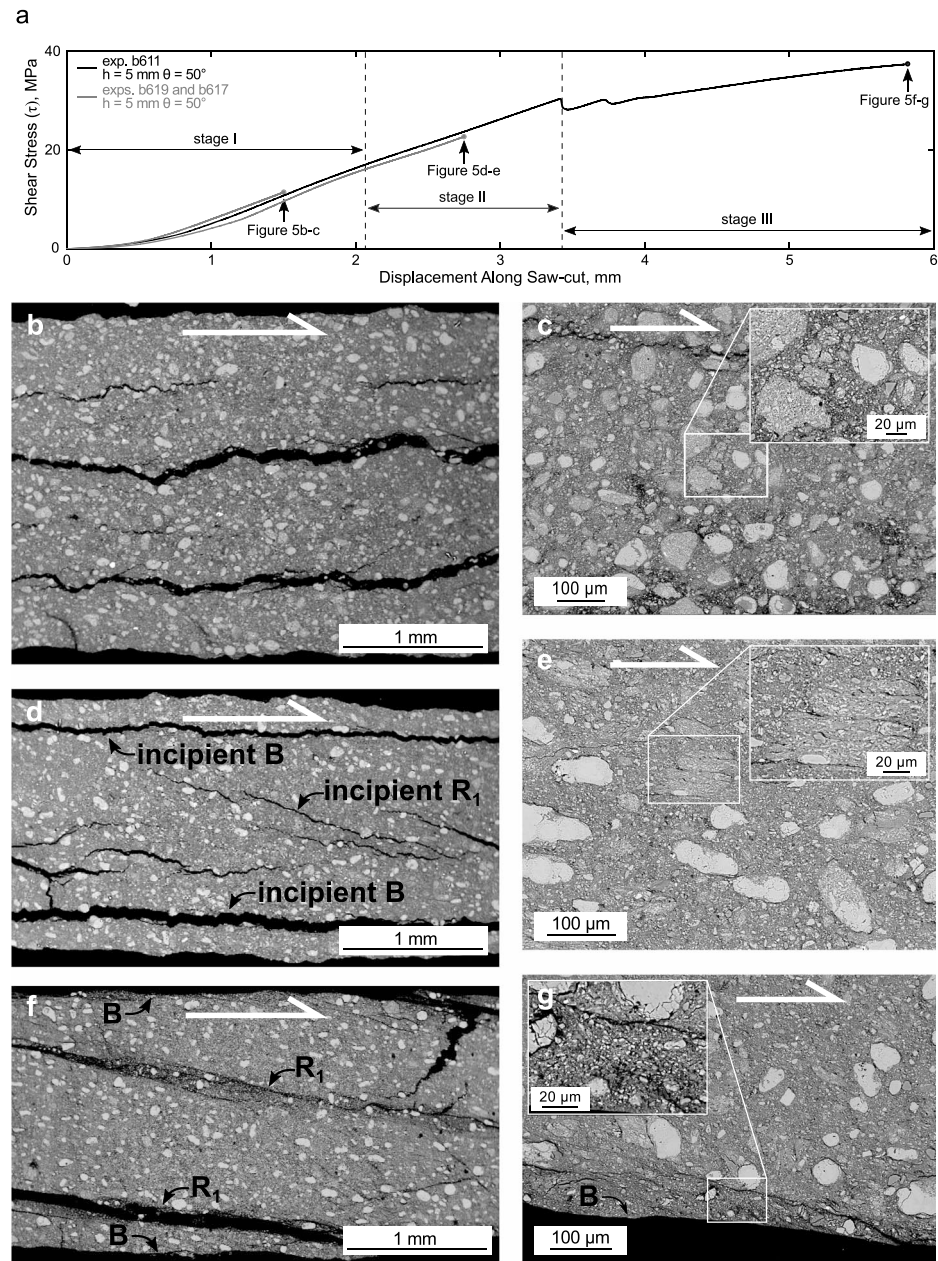


Figure 5. SEM (scanning electron microscope) micrograph showing microstructures developed in samples with different amount of total displacement. (a) Shear stress versus displacement along saw-cut plot showing at which displacement and during which stage microstructures were collected. (b) Microstructure after 1.5 mm of displacement along saw-cut (experiment b619, Table 1) characterized by isotropically distributed clasts of marl. (c) Detail of microstructure after 1.5 mm of displacement in Figure 5b showing marly clasts in a fine and loose matrix composed of clay flakes and calcareous nannofossils. The inset shows marly clasts which are angular and irregular in shape. (d) Microstructure after 2.75 mm of displacement along saw-cut (experiment b617, Table 1) characterized by elongated clasts oriented consistently with the shear direction and incipient boundary and Riedel shears. (e) Detail of microstructure after 2.75 mm of displacement in Figure 5d showing elongated clasts oriented accordingly to the shear direction. The inset shows a rounded clast in a dense and well-packed matrix. (f) Microstructure after ~6 mm of displacement along saw-cut (experiment b611, Table 1) characterized by localized Riedel (R_1) and boundary (B) shear bands (Logan et al., 1992). (g) Details of a boundary shear band in Figure 5f. The inset shows the concentration of fine clay and calcite fragments along the B shear band.

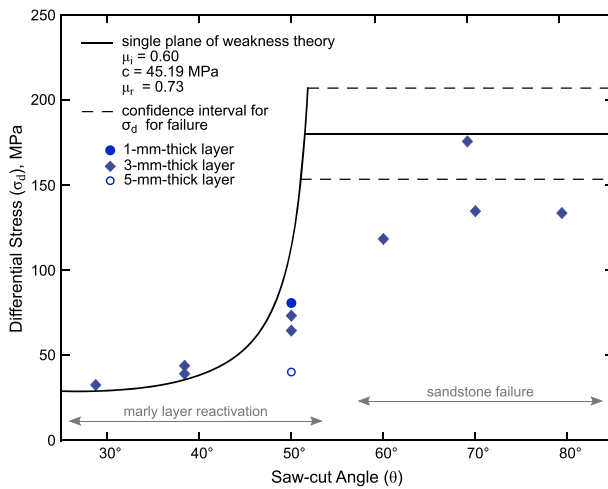


Figure 6. Results from triaxial saw-cut experiments compared with the single plane of weakness theory (equations (1) and (2)). The predicted sandstone strength is reported along with the confidence interval (two sided, 98%) calculated on the base of the residuals of the linear regression (Figure 2c). The maximum σ_d supported by triaxial saw-cut samples before fault reactivation or new fracture development is plotted against the saw-cut angle. Slip within the fault occurs for $\theta = 30^\circ\text{--}40^\circ\text{--}50^\circ$, whereas the development of a new fracture occurs for $\theta = 60^\circ\text{--}70^\circ\text{--}80^\circ$, in agreement with theoretical predictions. The σ_d required for reactivation differs from theoretical predictions.

experimentally derived values are picked as shown in Figure 1d. Particularly, the differential stress required for fault reactivation corresponds to the differential stress right before the stress drop, at the end of stage II (see section 4.1).

The range of reactivation angles of gouge-bearing faults is well predicted by the analytical model, which predicts frictional lock-up at $\theta = 51.5^\circ$, with fault slip for $\theta < 51.5^\circ$ and surrounding rock failure for $\theta > 51.5^\circ$ (Figure 6). Accordingly, samples with saw-cuts oriented at $\theta = 30^\circ\text{--}40^\circ\text{--}50^\circ$ experience fault reactivation, whereas for $\theta = 60^\circ\text{--}70^\circ\text{--}80^\circ$ new optimally oriented faults, often in conjugate sets, develop within the host rock (Figure 3b).

The differential stress for the failure of samples with severely misoriented faults (i.e., $\theta = 60^\circ\text{--}70^\circ\text{--}80^\circ$) in most of the cases is lower than model predictions. The elastic moduli variations as a function of the θ angle (Figure 3a) suggest that the gouge layer compaction, which depends on its orientation, influences the overall sample elasticity. Indeed, confining pressure being equal, more misoriented faults undergo higher normal stress increments, and thus higher compaction during loading, resulting in overall stiffer samples. Moreover, the development of a through-going fracture along with conjugate fractures could explain the occurrence of two or more stress drops during sample failure (Figure 3). We infer that the gouge layer initially accommodates the deformation by compacting through granular flow. When the stress is sufficiently high, a fracture develops in one of the two brittle sandstone halves (e.g., Welch et al.,

2009), resulting in a first stress drop, and subsequently propagates in the other sandstone half, resulting in a second stress drop (Figure 3). Consistently, further smaller stress drops are observed only in samples containing conjugate faults. The prefailure concentration of stress and strain within the gouge layer could also be responsible for the lower differential stress for failure with respect to the estimated sandstone strength. However, the high variability in differential stress for failure in both fault-bearing (Figures 3a and 6) and intact samples could also arise from the strength heterogeneity of the arkose sandstone (Figure 2c).

Coherent with the model, samples with saw-cuts oriented at $\theta = 30^\circ\text{--}40^\circ\text{--}50^\circ$ accommodate deformation via frictional reactivation of the preexisting fault (Figure 4a). However, fault reactivation occurs at levels of differential stress that are substantially different from theoretical predictions (Figure 6c). In particular, 3-mm-thick gouge layers require differential stresses that are higher than theoretically predicted at $\theta = 30^\circ\text{--}40^\circ$ and lower at $\theta = 50^\circ$, which is in line with the findings of previous triaxial experiments on gouge-filled saw-cut samples with variable θ (e.g., Rutter & Hackston, 2017; Savage et al., 1996). Remarkably, at $\theta = 50^\circ$, the differential stress necessary for the reactivation of the 1-mm-thick gouge layer (i.e., $\sigma_d \approx 80$ MPa) is twice the differential stress necessary for the reactivation of the 5-mm-thick gouge layer ($\sigma_d \approx 40$ MPa), suggesting that the layer thickness strongly influences the differential stress required for reactivation of the misoriented fault.

Microstructural observations suggest that fault shear deformation starts with distributed shear-enhanced compaction, which accommodates ≤ 2 mm of shear displacement (Figures 5b–5e). This granular flow promotes the progressive rotation of the maximum principal stress within the fault zone from its far-field orientation (i.e., from the vertical σ_1 imposed by the apparatus) to 45° to the boundary of the saw-cut within the gouge shear zone (e.g., Figures 7a and 7b, Byerlee & Savage, 1992; Lockner & Byerlee, 1993; Mandl et al., 1977). This stress rotation results in slightly higher differential stress for reactivation when $\theta < 45^\circ$ and significantly lower differential stress for $45^\circ < \theta < \text{fault lock-up}$ (Figures 7a–7c). Consequently, shear and normal stresses for reactivation are higher than predicted when $\theta < 45^\circ$ and lower than predicted at $\theta > 45^\circ$ (Figure 7b). Thus, the differential stress required for reactivation of a thick fault zone is modulated accordingly to the stress state developed within the gouge layer and, consequently, to whether the slip is distributed or localized during reactivation, and this is supported by experimental data (Figure 7c).

Additionally, at $\theta = 50^\circ$, we observe a significant decrease in the differential stress required for reactivation with increasing layer thickness. We relate this to the fact that the rotation of the stress field is more efficient

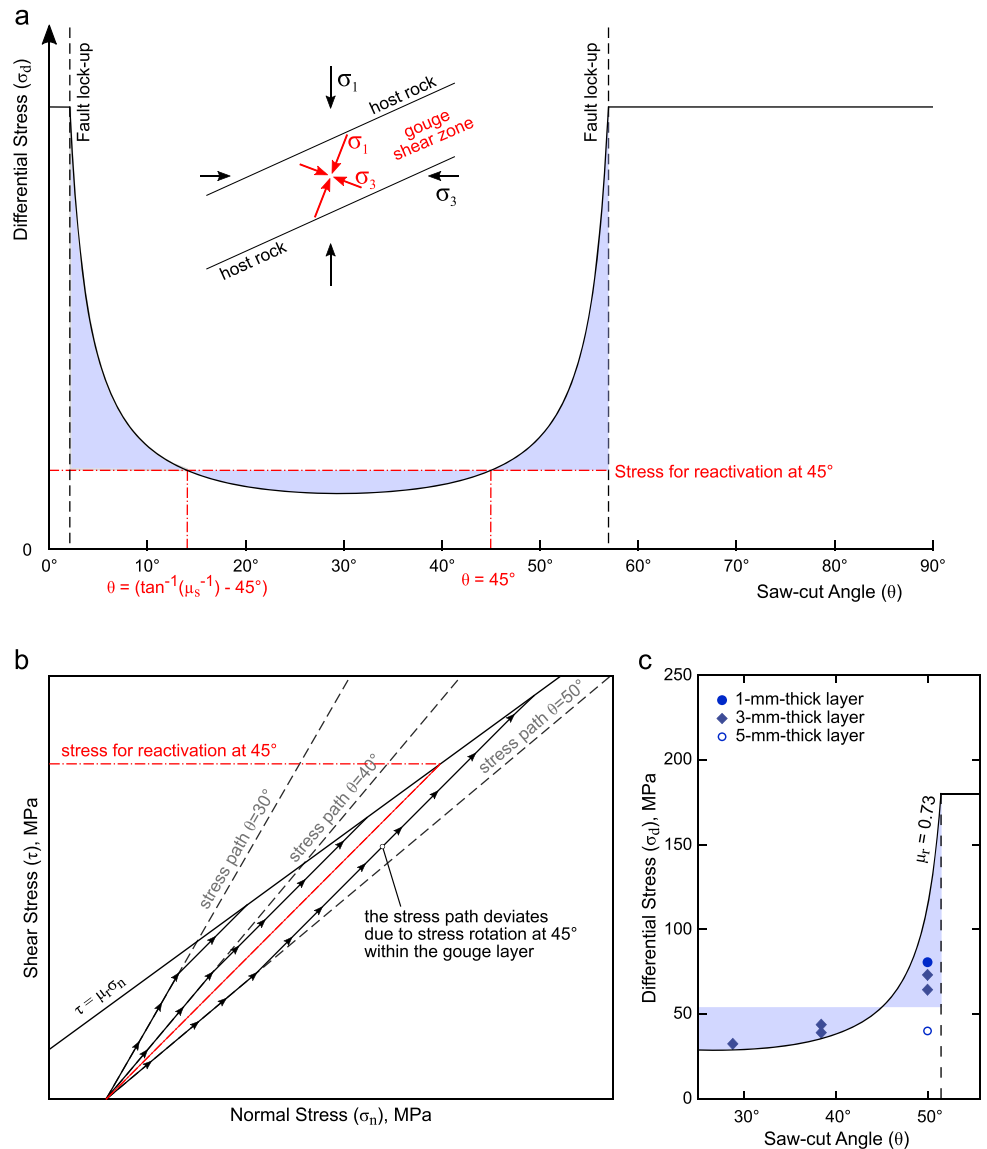


Figure 7. (a) Conceptual model for reactivation of gouge-bearing faults. Before reactivation, distributed deformation occurs and causes the progressive rotation of the stress field within the gouge. Thus, reactivation occurs accordingly to the stress state developed within the gouge. If the full stress rotation occurs, the differential stress for fault reactivation is independent on fault orientation and it is equal to the differential stress for reactivation at $\theta = 45^\circ$ (horizontal red dashed line). If the stress does not fully rotate, the fault reactivates at intermediate values of differential stress, between the far-field and the fully rotated stress state (blue shaded area). (b) Deviation of the stress path (lines with arrows) from the prediction based on far-field stress orientation (gray dashed line). This deviation results from stress field rotation at 45° to the boundary of the saw-cut. Faults oriented at $\theta = 30^\circ$ – 40° reactivate at shear stress higher than predicted but lower than the shear stress for reactivation at $\theta = 45^\circ$, whereas faults oriented at $\theta = 50^\circ$ reactivate at shear stress lower than predicted but higher than the shear stress for reactivation at $\theta = 45^\circ$. The stress path at $\theta = 45^\circ$ is reported as well. (c) The experimental data are in agreement with this conceptual model, and the increase in layer thickness further reduces the differential stress required for reactivation of a severely misoriented fault at $\theta = 50^\circ$.

within thicker gouge layers, as also outlined by the previous studies (e.g., Marone, 1995). The dependence of differential stress on gouge layer thickness has been previously documented (e.g., Anthony & Marone, 2005; Dieterich, 1981; Karner & Marone, 2001). Particularly, in our experiments, differential stress is sustained by the clast-supported fabric of the gouge layer. This clast-supported fabric contains a number of load-bearing contacts across the layer, which depends on the layer thickness. Consequently, a thicker layer contains a higher number of contacts resulting in more points of potential failure and, since the force is distributed

on a larger number of contacts, a thick layer supports lower differential stress than a thinner one (e.g., Anthony & Marone, 2005). Moreover, the 5-mm-thick fault reactivates for a differential stress value that approaches the minimum differential stress for reactivation, suggesting the possible development of newly favorably oriented shear fractures within the gouge layer.

4.3. Implications for Natural Faults

Predictions based on the frictional fault reactivation theory (e.g., Sibson, 1985) have been used to give a first-order interpretation of the dip distribution of moderate and large earthquakes occurring in the intracontinental crust (Collettini & Sibson, 2001) or to characterize the strength of the brittle crust (Townend & Zoback, 2000). In this work, we experimentally validated the applicability of the frictional fault reactivation theory (e.g., Sibson, 1985) for gouge-bearing faults, showing that the theoretically predicted fault lock-up angle controls the occurrence of reactivation versus the formation of a new optimally oriented fault within the applied stress field (Figure 6). Beyond confirming this first-order prediction, our experiments also highlight that the differential stress for reactivation might significantly differ from analytical predictions, with strong implications for the evaluation of the reactivation potential of preexisting faults. A strong assumption of this analytical approach is that faults are planes of weakness, characterized by zero thickness, whose reactivation is controlled by their friction (e.g., Morris et al., 1996; Sibson, 1985). Though such an assumption seems reasonable at crustal scale, natural faults are not zero-thickness surfaces and host more or less thick fault cores and damage zones (e.g., Ben-Zion & Sammis, 2003; Caine et al., 1996; Choi et al., 2016). Our results highlight that the presence of fault gouge and its mode of deformation strongly control the amount of stress required for reactivation (Figure 7). We document that the gouge promotes the reorientation of the far-field stress at 45° to the fault plane. Our conceptual model suggests that the stress rotation within the fault gouge weakens unfavorably oriented faults that lie at angles between $\theta = 45^\circ$ and the frictional lock-up. For these fault orientations, the assumption of a zero-thickness, planar fault provides only an upper bound on the stress required for reactivation, possibly leading to an overestimation of fault strength. In natural faults, stress rotation is proven by seismological observations (e.g., Hardebeck & Hauksson, 1999; Provost & Houston, 2001), supported by theoretical models (e.g., Rice, 1992; Scholz, 2000), and claimed to be an effective mechanism to enhance slip along misoriented faults (e.g., Axen, 1992; Rice, 1992).

5. Conclusions

We investigated the reactivation of preexisting gouge-bearing faults at a different orientation to the maximum principal stress, simulating experimental faults from optimally oriented to severely misoriented for reactivation. We experimentally validate the frictional lock-up for gouge-bearing faults, reporting that the reactivation is mainly controlled by the interplay between the friction of the gouge and the strength of the surrounding sandstone. However, the differential stress required for reactivation strongly differs from theoretical predictions, especially for unfavorably oriented gouge-bearing faults that appear systematically weaker. We ascribe this weakening to the rotation of the maximum principal stress within the gouge layer during distributed deformation, which precedes reactivation. Our results also show that the thickness of the fault gouge reduces the differential stress for reactivation. As applied to tectonic faults, we suggest that thick shear zones of distributed deformation might be weaker than theoretically predicted.

Acknowledgments

The authors are grateful to D. Mannetta for high-quality thin section preparation and to M. Nazzari and M. Albano for assistance with the SEM (scanning electron microscope). The authors thank EPFL (École Polytechnique Fédérale de Lausanne) for profilometer analyses. M. Mercuri is thanked for fruitful discussions. This research was funded by the ERC Starting Grant GLASS project (259256) and Fondi Ateneo Sapienza 2016 to C. Collettini. We thank an anonymous reviewer and the Associate Editor whose comments helped strengthen this manuscript. The data that support the findings of this study are openly available in Mendeley Data at <https://doi.org/doi:10.17632/ny8w37pf6y.1>. In addition, all the data are available upon request to the corresponding author.

References

- Anthony, J. L., & Marone, C. (2005). Influence of particle characteristics on granular friction. *Journal of Geophysical Research*, *110*, B08409. <http://doi.org/doi:10.1029/2004JB003399>
- Axen, G. J. (1992). Pore pressure, stress increase, and fault weakening in low-angle normal faulting. *Journal of Geophysical Research*, *97*(B6), 8979–8991. <http://doi.org/doi:10.1029/92JB00517>
- Barchi, M., Landuzzi, A., Minelli, G., & Pialli, G. (2001). Outer northern Apennines. In G. Vai & I. Martini (Eds.), *Anatomy of an orogen: The Apennines and adjacent Mediterranean basins* (pp. 215–254). Netherlands: Springer. https://doi.org/10.1007/978-94-015-9829-3_15
- Benson, P. M., Thompson, B. D., Meredith, P. G., Vinciguerra, S., & Young, R. P. (2007). Imaging slow failure in triaxially deformed Etna basalt using 3D acoustic-emission location and X-ray computed tomography. *Geophysical Research Letters*, *34*, L03303. <http://doi.org/doi:10.1029/2006GL028721>
- Ben-Zion, Y., & Sammis, C. G. (2003). Characterization of fault zones. *Pure and Applied Geophysics*, *160*(3), 677–715. <http://doi.org/doi:10.1007/PL00012554>
- Biegel, R. L., Sammis, C. G., & Dieterich, J. H. (1989). The frictional properties of a simulated gouge having a fractal particle distribution. *Journal of Structural Geology*, *11*(7), 827–846. [http://doi.org/doi:10.1016/0191-8141\(89\)90101-6](http://doi.org/doi:10.1016/0191-8141(89)90101-6)

- Bolognesi, F., & Bistacchi, A. (2016). Weakness and mechanical anisotropy of phyllosilicate-rich cataclases developed after mylonites of a low-angle normal fault (Simplon Line, western Alps). *Journal of Structural Geology*, *83*, 1–12. <http://doi.org/doi:10.1016/j.jsg.2015.11.009>
- Bowden, F. P., & Tabor, D. (1950). *Friction and lubrication of solids*. New York, NY: Oxford Univ. Press.
- Brace, W. F., Paulding, B. W., & Scholz, C. (1966). Dilatancy in the fracture of crystalline rocks. *Journal of Geophysical Research*, *71*(16), 3939–3953. <http://doi.org/doi:10.1029/JZ071i016p03939>
- Byerlee, J. D., & Savage, J. C. (1992). Coulomb plasticity within the fault zone. *Geophysical Research Letters*, *19*(23), 2341–2344. <http://doi.org/doi:10.1029/92GL02370>
- Caine, J. S., Evans, J. P., & Forster, C. B. (1996). Fault zone architecture and permeability structure. *Geology*, *24*(11), 1025–1028. [http://doi.org/doi:10.1130/0091-7613\(1996\)024<1025:FZAAPS>2.3.CO;2](http://doi.org/doi:10.1130/0091-7613(1996)024<1025:FZAAPS>2.3.CO;2)
- Choi, J. H., Edwards, P., Ko, K., & Kim, Y. S. (2016). Definition and classification of fault damage zones: A review and a new methodological approach. *Earth-Science Reviews*, *152*, 70–87. <https://doi.org/10.1016/j.earscirev.2015.11.006>
- Coccioni, R., Franchi, R., Nesci, O., Perilli, N., Wezel, F. C., & Battistini, F. (1989). Stratigrafia, micropaleontologia e mineralogia delle Marne a Fucoidi (Aptiano inferiore-Albiano superiore) delle sezioni di Poggio le Guaine e del Fiume Bosso (Appennino umbromarchigiano). In G. Pallini, F. Cecca, S. Cresta & M. Santantonio (Eds.), *Atti del secondo convegno internazionale, Fossili, Evoluzione, Ambiente* (pp. 163–201). Pergola, Italy.
- Colletini, C., Di Stefano, G., Carpenter, B. M., Scarlato, P., Tesei, T., Mollo, S., et al. (2014). A novel and versatile apparatus for brittle rock deformation. *International Journal of Rock Mechanics and Mining Sciences*, *66*, 114–123. <https://doi.org/doi:10.1016/j.ijrmm.2013.12.005>
- Colletini, C., & Sibson, R. H. (2001). Normal faults normal friction? *Geology*, *29*(10), 927–930. [https://doi.org/10.1130/0091-7613\(2001\)029<0927:NFNF>2.0.CO;2](https://doi.org/10.1130/0091-7613(2001)029<0927:NFNF>2.0.CO;2)
- Colletini, C., & Trippetta, F. (2007). A slip tendency analysis to test mechanical and structural control on aftershock rupture planes. *Earth and Planetary Science Letters*, *255*(3–4), 402–413. <https://doi.org/doi:10.1016/j.epsl.2007.01.001>
- Colletini, C., Viti, C., Smith, S. A. F., & Holdsworth, R. E. (2009). Development of interconnected talc networks and weakening of continental low-angle normal faults. *Geology*, *37*(6), 567–570. <https://doi.org/10.1130/G25645A.1>
- Copley, A. (2017). The strength of earthquake-generating faults. *Journal of the Geological Society*, *175*(1), 1–12. <https://doi.org/doi:10.1144/jgs2017-037>
- Coulomb, C. A. (1776). Sur une application des réglés maximis et minimis a quelques problèmes de statique, relatifs à l'architecture. *Mémoires de Mathématique et de Physique de l'Académie Royale de Sciences*, *7*, 343–382.
- Dieterich, J. H. (1981). Constitutive properties of faults with simulated gouge. In N. L. Carter, M. Friedman, J. M. Logan, & D. W. Stearns (Eds.), *Mechanical behavior of crustal rocks: The Handin volume* (pp. 103–120). Washington, DC: American Geophysical Union. <https://doi.org/doi:10.1029/GM024p0103>
- Donath, F. A. (1961). Experimental study of shear failure in anisotropic rocks. *Geological Society of America Bulletin*, *72*(6), 985–989. [https://doi.org/10.1130/0016-7606\(1961\)72\[985:ESOSFI\]2.0.CO;2](https://doi.org/10.1130/0016-7606(1961)72[985:ESOSFI]2.0.CO;2)
- Ellsworth, W. L. (2013). Injection-induced earthquakes. *Science*, *341*(6142), 1225–1229. <https://doi.org/doi:10.1126/science.1225942>
- Faulkner, D. R., Mitchell, T. M., Jensen, E., & Cembrano, J. (2011). Scaling of fault damage zones with displacement and the implications for fault growth processes. *Journal of Geophysical Research*, *116*, B05403. <https://doi.org/10.1029/2010JB007788>
- Fratini, F., Pecchioni, E., Cantisani, E., Rescic, S., & Vettori, S. (2014). Pietra Serena: The stone of the Renaissance. *Geological Society of London, Special Publication*, *407*(1), 173–186. <https://doi.org/doi:10.1144/SP407.11>
- Gan, Q., & Elsworth, D. (2014). Analysis of fluid injection-induced fault reactivation and seismic slip in geothermal reservoirs. *Journal of Geophysical Research: Solid Earth*, *119*, 3340–3353. <https://doi.org/10.1002/2013JB010679>
- Giorgetti, C., Colletini, C., Scuderi, M. M., Barchi, M. R., & Tesei, T. (2016). Fault geometry and mechanics of marly carbonate multilayers: An integrated field and laboratory study from the northern Apennines, Italy. *Journal of Structural Geology*, *93*, 1–16. <https://doi.org/doi:10.1016/j.jsg.2016.10.001>
- Gu, Y., & Wong, T.-F. (1994). Development of shear localization in simulated quartz gouge: Effect of cumulative slip and gouge particle size. *Pure and Applied Geophysics*, *143*(1–3), 387–423. <https://doi.org/10.1007/BF00874336>
- Hardebeck, J., & Hauksson, E. (1999). Role of fluids in faulting inferred from stress field signatures. *Science*, *285*(5425), 236–239. <https://doi.org/doi:10.1126/science.285.5425.236>
- Harris, R. A., & Simpson, R. W. (1992). Changes in static stress on Southern California faults after the 1992 Landers earthquake. *Nature*, *360*(6401), 251–254. <https://doi.org/10.1038/360251a0>
- Hayward, K. S., & Cox, S. F. (2017). Melt welding and its role in fault reactivation and localization of fracture damage in seismically active faults. *Journal of Geophysical Research: Solid Earth*, *122*, 9689–9713. <https://doi.org/doi:10.1002/2017JB014903>
- Hoek, E. (1964). Fracture of anisotropic rock. *Journal of the South African Institute of Mining and Metallurgy*, *64*(10), 501–523.
- Jackson, R. E., & Dunn, D. E. (1974). Experimental sliding friction and cataclasis of foliated rocks. *International Journal of Rock Mechanics and Mining Sciences*, *11*(6), 235–249. [https://doi.org/doi:10.1016/0148-9062\(74\)90130-2](https://doi.org/doi:10.1016/0148-9062(74)90130-2)
- Jaeger, J. C. (1960). Shear failure of anisotropic rocks. *Geological Magazine*, *97*(01), 65–72. <https://doi.org/doi:10.1017/S0016756800061100>
- Jaeger, J. C., & Cook, N. G. W. (1979). *Fundamentals of rock mechanics* (3rd ed.). New York, NY: Chapman and Hall.
- Karner, S. L., & Marone, C. (2001). Fractional restrengthening in simulated fault gouge: Effect of shear load perturbations. *Journal of Geophysical Research*, *106*(B9), 19,319–19,337. <https://doi.org/10.1029/2001JB000263>
- Lacroix, B., Tesei, T., Oliot, E., Lahfid, A., & Colletini, C. (2015). Early weakening processes inside thrust fault. *Tectonics*, *34*, 1396–1411. <https://doi.org/doi:10.1002/2014TC003716>
- Leclère, H., & Fabbri, O. (2013). A new three-dimensional method of fault reactivation analysis. *Journal of Structural Geology*, *33*(10), 1900–1919. <https://doi.org/doi:10.1002/2014TC003600>
- Lecomte, E., Le Pourhiet, L., Lacombe, O., & Jolivet, L. (2011). A continuum mechanics approach to quantify brittle strain on weak faults: Application to the extensional reactivation of shallow dipping discontinuities. *Geophysical Journal International*, *184*(1), 1–11. <https://doi.org/doi:10.1111/j.1365-246X.2010.04821.x>
- Lecomte, E., Le Pourhiet, L., & Lacombe, O. (2012). Mechanical basis for slip along low-angle normal faults. *Geophysical Research Letters*, *39*, L03307. <https://doi.org/doi:10.1029/2011GL050756>
- Lisle, R. J., & Srivastava, D. C. (2004). Test of the frictional reactivation theory for faults and validity of fault-slip analysis. *Geology*, *32*(7), 569–572. <https://doi.org/doi:10.1130/G20408.1>

- Lockner, D. A., & Byerlee, J. D. (1993). How geometrical constraints contribute to the weakness of mature faults. *Nature*, *363*(6426), 250–252. <https://doi.org/doi:10.1038/363250a0>
- Lockner, D. A., Byerlee, J. D., Kuksenko, W., Ponomarev, A., & Sidorin, A. (1992). Observations of quasistatic fault growth from acoustic emissions. In B. Evans & T.-F. Wong (Eds.), *Fault mechanics and transport properties of rocks—A Festschrift in honor of W. F. Brace* (pp. 3–31). San Diego, CA: Academic. [https://doi.org/doi:10.1016/S0074-6142\(08\)62813-2](https://doi.org/doi:10.1016/S0074-6142(08)62813-2)
- Logan, J. M., Dengo, C. A., Higgs, N. G., & Wang, Z. Z. (1992). Fabric of experimental fault zone: Their development and relationship to mechanical behavior. In B. Evans & T.-F. Wong (Eds.), *Fault mechanics and transport properties of rocks—A Festschrift in honor of W. F. Brace* (pp. 33–67). San Diego, CA: Academic. [https://doi.org/doi:10.1016/S0074-6142\(08\)62814-4](https://doi.org/doi:10.1016/S0074-6142(08)62814-4)
- Mandl, G., de Jong, L. N. J., & Maltha, A. (1977). Shear zones in granular material: An experimental study of their structure and mechanical genesis. *Rock Mechanics*, *9*(2-3), 95–144. <https://doi.org/doi:10.1007/BF01237876>
- Marone, C. (1995). Fault zone strength and failure criteria. *Geophysical Research Letters*, *22*(6), 723–726. <https://doi.org/doi:10.1029/95GL00268>
- Marone, C., Hobbs, B. E., & Ord, A. (1992). Coulomb constitutive laws for friction: Contrasts in frictional behavior for distributed and localized shear. *Pure and Applied Geophysics*, *139*(2), 195–214. <https://doi.org/doi:10.1007/BF00876327>
- McCabe, W., & Koerner, R. M. (1975). High pressure shear strength investigation of an anisotropic mica schist rock. *International Journal of Rock Mechanics and Mining Sciences*, *12*(8), 219–228. [https://doi.org/doi:10.1016/0148-9062\(75\)91402-3](https://doi.org/doi:10.1016/0148-9062(75)91402-3)
- McLamore, R., & Gray, K. (1967). The mechanical behavior of anisotropic sedimentary rocks. *Journal of Engineering for Industry*, *89*(1), 62–73. <https://doi.org/doi:10.1115/1.3610013>
- Moock, I., Kwiatek, G., & Zimmermann, G. (2009). Slip tendency analysis, fault reactivation potential and induced seismicity in a deep geothermal reservoir. *Journal of Structural Geology*, *31*(10), 1174–1182. <https://doi.org/10.1016/j.jsg.2009.06.012>
- Morris, A., Ferrill, D. A., & Henderson, D. B. (1996). Slip-tendency analysis and fault reactivation. *Geology*, *24*(3), 275–278. [https://doi.org/doi:10.1130/0091-7613\(1996\)024<0275:STAAFR>2.3.CO;2](https://doi.org/doi:10.1130/0091-7613(1996)024<0275:STAAFR>2.3.CO;2)
- Paterson, M. S., & Wong, T.-F. (2005). *Experimental rock deformation—The brittle field* (2nd ed.). New York, NY: Springer.
- Provost, A. S., & Houston, H. (2001). Orientation of the stress field surrounding the creeping section of the San Andreas fault: Evidence for a narrow mechanically weak fault zone. *Journal of Geophysical Research*, *106*(B6), 11,373–11,386. <https://doi.org/doi:10.1029/2001JB900007>
- Rice, J. R. (1992). Fault stress states, pore pressure distributions and the weakness of the San Andreas fault. In B. Evans & T.-F. Wong (Eds.), *Fault mechanics and transport properties of rocks—A Festschrift in honor of W. F. Brace* (pp. 475–503). San Diego, CA: Academic. [https://doi.org/doi:10.1016/S0074-6142\(08\)62835-1](https://doi.org/doi:10.1016/S0074-6142(08)62835-1)
- Rutqvist, J., Birkholzer, J., Cappa, F., & Tsang, C.-F. (2007). Estimating maximum sustainable injection pressure during sequestration of CO₂ using coupled fluid flow and geomechanical fault-slip analysis. *Energy Conversion and Management*, *48*(6), 1798–1807. <https://doi.org/doi:10.1016/j.enconman.2007.01.021>
- Rutter, E., & Hackston, A. (2017). On the effective stress law for rock-on-rock frictional sliding, and fault slip triggered by means of fluid injection. *Philosophical Transactions of the Royal Society A*, *375*(2103), 20160001. <https://doi.org/doi:10.1098/rsta.2016.0001>
- Savage, J. C., Lockner, D. A., & Byerlee, J. D. (1996). Failure of laboratory fault models in triaxial tests. *Journal of Geophysical Research*, *101*(B10), 22,215–22,224. <https://doi.org/doi:10.1029/96JB02094>
- Schoenball, M., Walsh, F. R., Weingarten, M., & Ellsworth, W. L. (2018). How faults wake up: The Guthrie-Langston, Oklahoma earthquakes. *The Leading Edge*, *37*(2), 100–106. <https://doi.org/doi:10.1190/le37020100.1>
- Scholz, C. H. (2000). Evidence for a strong San Andreas fault. *Geology*, *28*(2), 163–166. [https://doi.org/doi:10.1130/0091-7613\(2000\)28<163:EFASSA>2.0.CO;2](https://doi.org/doi:10.1130/0091-7613(2000)28<163:EFASSA>2.0.CO;2)
- Scott, D. R., Lockner, D. A., Byerlee, J. D., & Sammis, C. G. (1994). Triaxial testing of Lopez fault gouge at 150 MPa mean effective stress. *Pure and Applied Geophysics*, *142*(3–4), 749–775. <https://doi.org/doi:10.1007/BF00876063>
- Scott, D. R., Marone, C., & Sammis, C. G. (1994). The apparent friction of granular fault gouge in sheared layers. *Journal of Geophysical Research*, *99*(B4), 7231–7246. <https://doi.org/doi:10.1029/93JB03361>
- Scuderi, M. M., & Colletini, C. (2016). The role of fluid pressure in induced vs. triggered seismicity: Insights from rock deformation experiments on carbonates. *Scientific Reports*, *6*(1), 24852. <https://doi.org/doi:10.1038/srep24852>
- Shea, T. W., & Kronenberg, A. K. (1993). Strength and anisotropy of foliated rocks with varied mica contents. *Journal of Structural Geology*, *15*(9–10), 1097–1121. [https://doi.org/doi:10.1016/0191-8141\(93\)90158-7](https://doi.org/doi:10.1016/0191-8141(93)90158-7)
- Shipton, Z. K., Soden, A. M., Kirkpatrick, J. D., Bright, A. M., & Lunn, R. J. (2006). How thick is a fault? Fault displacement-thickness scaling revisited. In R. E. Abercrombie, A. McGarr, H. Kanamori, & G. Di Toro (Eds.), *Earthquakes: Radiated energy and the physics of faulting*, *Geophysical Monograph Series* (Vol. 170, pp. 193–198). Washington, DC: American Geophysical Union. <https://doi.org/doi:10.1029/170GM19>
- Sibson, R. H. (1985). A note on fault reactivation. *Journal of Structural Geology*, *7*(6), 751–754. [https://doi.org/doi:10.1016/0191-8141\(85\)90150-6](https://doi.org/doi:10.1016/0191-8141(85)90150-6)
- Streit, J. E., & Hillis, R. R. (2004). Estimating fault stability and sustainable fluid pressures for underground storage of CO₂ in porous rock. *Energy*, *29*(9–10), 1445–1456. <https://doi.org/doi:10.1016/j.energy.2004.03.078>
- Sumy, D. F., Cochran, E. S., Keranen, K. M., Wei, M., & Abers, G. A. (2014). Observations of static Coulomb stress triggering of the November 2011 M5.7 Oklahoma earthquake sequence. *Journal of Geophysical Research: Solid Earth*, *119*, 1904–1923. <https://doi.org/doi:10.1002/2013JB010612>
- Tchalenko, J. S. (1970). Similarities between shear zones of different magnitudes. *Geological Society of America Bulletin*, *81*(6), 1625–1640. [https://doi.org/doi:10.1130/0016-7606\(1970\)81\[1625:SBSZOD\]2.0.CO;2](https://doi.org/doi:10.1130/0016-7606(1970)81[1625:SBSZOD]2.0.CO;2)
- Thompson, B. D., Young, R. P., & Lockner, D. A. (2006). Fracture in westerly granite under AE feedback and constant strain rate loading: Nucleation, quasi-static propagation, and the transition to unstable fracture propagation. *Pure and Applied Geophysics*, *163*(5–6), 995–1019. <https://doi.org/doi:10.1007/s00024-006-0054-x>
- Thompson, P. A., & Grest, G. S. (1991). Granular flow: Friction and the dilatancy transition. *Physical Review Letters*, *67*(13), 1751–1754. <https://doi.org/doi:10.1103/PhysRevLett.67.1751>
- Townend, J., & Zoback, M. D. (2000). How faulting keeps the crust strong. *Geology*, *28*(5), 399–402. [https://doi.org/doi:10.1130/0091-7613\(2000\)28<399:HFKTCS>2.0.CO;2](https://doi.org/doi:10.1130/0091-7613(2000)28<399:HFKTCS>2.0.CO;2)
- Walsh, F. R., & Zoback, M. D. (2016). Probabilistic assessment of potential fault slip related to injection induced earthquakes: Application to north central Oklahoma, USA. *Geology*, *44*(12), 991–994. <https://doi.org/doi:10.1130/G38275.1>
- Welch, M. J., Davies, R. K., Knipe, R. J., & Tueckmantel, C. (2009). A dynamic model for fault nucleation and propagation in a mechanically layered section. *Tectonophysics*, *474*(3–4), 473–492. <https://doi.org/doi:10.1016/j.tecto.2009.04.025>

- Wiprut, D., & Zoback, M. D. (2002). Fault reactivation, leakage potential, and hydrocarbon column heights in the northern North Sea. In A. G. Koestler & R. Hunsdale (Eds.), *Hydrocarbon seal quantification* (pp. 203–219). Amsterdam: Elsevier. [https://doi.org/doi:10.1016/S0928-8937\(02\)80016-9](https://doi.org/doi:10.1016/S0928-8937(02)80016-9)
- Wong, T.-F., David, C., & Zhu, W. (1997). The transition from brittle faulting to cataclastic flow in porous sandstones: Mechanical deformation. *Journal of Geophysical Research*, *102*(B2), 3009–3025. <https://doi.org/doi:10.1029/96JB03281>
- Wood, D. M. (1990). *Soil behaviour and critical state soil mechanics*. Cambridge, NY: Cambridge Univ. Press.